

# Variational-State Quantum Metrology

Bálint Koczor<sup>1</sup>, Suguru Endo<sup>1</sup>, Tyson Jones<sup>1</sup>, Yuichiro Matsuzaki<sup>2</sup>, Simon C. Benjamin<sup>1</sup>

<sup>1</sup>Department of Materials, University of Oxford, Parks Road, Oxford OX1 3PH, United Kingdom

**Abstract.** Quantum technologies exploit entanglement to enhance various tasks beyond their classical limits including computation, communication and measurements. Quantum metrology aims to increase the precision of a measured quantity that is estimated in the presence of statistical errors using entangled quantum states. We present a novel approach for finding (near) optimal states for metrology in the presence of noise, using variational techniques as a tool for efficiently searching the classically intractable high-dimensional space of quantum states. We comprehensively explore systems consisting of up to 9 qubits and find new highly entangled states that are not symmetric under permutations and non-trivially outperform previously known states up to a constant factor 2. We consider a range of environmental noise models; while passive quantum states cannot achieve a fundamentally superior scaling (as established by prior asymptotic results) we do observe a significant absolute quantum advantage. We finally outline a possible experimental setup for variational quantum metrology which can be implemented in near-term hardware.

## 1. Introduction

Variational quantum algorithms (VQAs) are potentially powerful for solving various problems using near-term quantum computers [1, 2, 3, 4, 5, 6]. These techniques can be implemented on shallow-depth quantum circuits that depend on external parameters and these parameters are typically optimised externally by a classical computer. Moreover, variational quantum algorithms are expected to be the first applications of quantum computers that could potentially outperform the best classical computers in practically relevant tasks.

Variational quantum circuits by construction depend only on a linear or polynomial number of parameters while the Hilbert-space dimension of the underlying quantum state increases exponentially in the number of qubits. This advantageous scaling allows one to tackle classically intractable problems. The general concept of variational quantum algorithms is to prepare a parametrised quantum state using a quantum processor and to vary its parameters externally until the optimum of a suitable cost function is reached. This cost function can be tailored to the particular problem. For example, one can search for the ground state of a molecule by setting the cost function to be the expectation value of the corresponding molecular Hamiltonian. This technique is

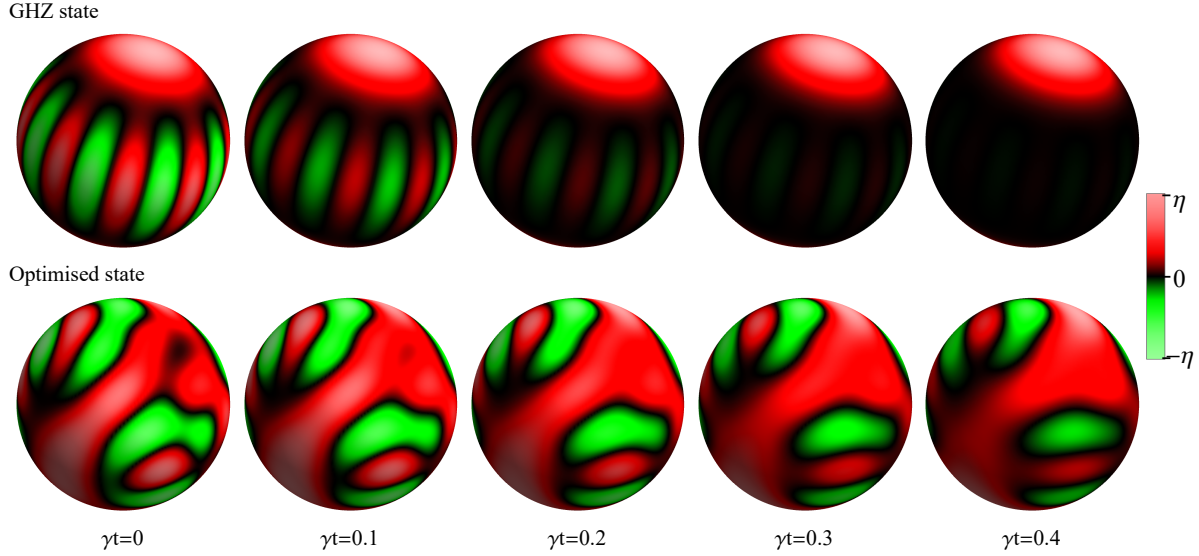


**Figure 1.** Wigner functions of permutation-symmetric 9-qubit quantum states that evolve under dephasing noise. Time increases left-to-right and  $\gamma t$  is the dimensionless time expressed in units of the decay time  $\gamma^{-1}$ . GHZ (upper) states are the most sensitive to an external magnetic field, but their coherences rapidly deteriorate due to fluctuations of the external field (as can be inferred from the rapidly fading coherences in their Wigner functions). Our aim in the current work is to find states (lower) that are optimally sensitive to the external field while being robust against noise using variational techniques. These optimal states are not necessarily permutation symmetric (refer to Sec. 5.3). Red and green colours show positive and negative values of the function while brightness represents the absolute value of the function relative to its global maximum  $\eta$ .

usually referred to as the variational quantum eigensolver (VQE) [1, 2, 3, 4]. Quantum machine learning is another area where variational techniques may be valuable. One is then interested in optimising a cost function that quantifies how similar the output of the quantum circuit is to a fixed dataset [7, 8]. Moreover, it is also possible to recompile a quantum circuit into another by optimising a metric on related quantum states [9, 10].

On the other hand, quantum metrology aims to enhance the precision of a measurement process in the presence of statistical errors using entangled quantum states [11, 12, 13, 14]. For example, sensing magnetic fields with high precision is crucial in many applications, such as determining chemical structure [15] or imaging living cells [16]. Various different types of high-performance magnetic field sensors have been developed, including hall-effect sensors [17], superconducting quantum interference devices (SQUID) [18] and force sensors [19]. In particular, in case of qubit-based magnetic field sensors, a qubit system interacts with the magnetic field and the information about the magnetic field is encoded as an internal relative phase of the quantum state. This information can then be extracted via a Ramsey-type measurement [20, 21, 22] that uses repeated projective measurements. These experiments need to be iterated a number of times in order to decrease the effect of statistical errors, such as the so-called shot noise.

If the probe state used in a metrology experiment is an unentangled qubit state, the estimation error of the external magnetic field (after a given number  $\nu$  of fixed-duration field sampling experiments) is proportional to  $\nu^{-1/2}$ . This scaling of the precision is often referred to as the standard quantum limit (SQL) [11, 12, 13, 14] and can potentially be enhanced by using certain entangled states such as GHZ states, symmetric Dicke states or squeezed states. Although these entangled states offer a scaling of the estimation error beyond the standard quantum limit  $\nu^{-c}$  with  $1/2 \leq c \leq 1$ , they are also sensitive to noise as illustrated in Fig. 1. In particular, it is well known that in the presence of uncorrelated Markovian dephasing, the scaling achieved with a GHZ state is only the standard quantum limit [23]. It is our aim in the current work to derive quantum states that are robust to environmental noise but also sensitive to the external field of interest. It is known from prior studies that quantum states subject to noise do not offer an improved fundamental scaling [24, 25, 12, 26, 27] unless they are actively corrected during the environmental interaction [28, 29, 30, 31, 32, 33, 34, 35, 36]. Nevertheless, optimisations of particular probe states show that a significant improvement as a constant absolute factor [23, 37, 12] can be gained, even without active error correction.

Here, we propose a new variational quantum algorithm that optimises parametrised probe states via a cost function that quantifies the metrological usefulness of a quantum state, i.e., the precision of estimating the external field (refer to Sec. 3). In particular, we envisage a quantum device that can generate a probe state using a variational quantum circuit and this probe state can interact with the external field of interest. We take into account the simultaneous effect of decoherence due to environmental noise that deteriorates the information about the external field contained in the probe state. Finally, the output state is measured in a suitable measurement basis to obtain the relevant cost function in a post-processing step, and the parameters of the quantum circuit are updated accordingly. This procedure is repeated until the optimal quantum state is found that achieves the highest sensitivity under a given noise model that is specific to the particular implementation of the device. Note that available noisy quantum computer hardware, such as superconducting qubits, can be straightforwardly used in this task either with or without error mitigation or error correction.

We numerically simulate experiments under various different error models in Sec 4 and comprehensively explore systems consisting of up to 9 qubits. We find families of quantum states that non-trivially outperform previously known states. In particular, our quantum algorithm searches within the exponentially large space of non-symmetric states (as opposed to the linear dimensionality of symmetric ones) and can therefore more fully exploit the potential offered by universal quantum computers. We find that relaxing permutation symmetry offers a significant improvement of the metrological sensitivity beyond symmetric states. This is a very interesting discovery and, perhaps, counter-intuitive as the problem of sensing an external field under environmental noise (as in Eq. 8) is symmetric under permutations and, to our best knowledge, states reported so far in the context of quantum metrology are also symmetric [23, 38, 39, 40, 41, 42, 43] e.g., GHZ, squeezed or symmetric Dicke states [14, 12].

And note that those permutation symmetric states are indeed optimal in the noise-free scenario. We develop an analytical understanding of a new family of highly entangled states that are not symmetric under permutations but significantly outperform their symmetric analogues under experimental noise: We derive an analytical model to show that these states can passively correct first-order decay events of the amplitude damping channel and hence their superior performance. We emphasise that our aim in this work is to find practically relevant (near) optimal states of a small number of qubits  $N$  that can be implemented in near term quantum hardware as opposed to finding asymptotically optimal states (i.e., when  $N \rightarrow \infty$ ).

Furthermore, our algorithm is also practically useful for the following reasons. First, in contrast to previous approaches which assumed and were limited to specific noise models to maximise the metrological performance [38, 39, 40, 41, 42, 43], our algorithm is independent of the choice of particular noise models. In particular, we assume a fixed quantum hardware and our algorithm by construction finds the metrologically optimal state that is tailored to the imperfections of that given device. Moreover, our quantum measurement device can be implemented on near-term quantum computers even without using quantum process tomography (which aims to identify the dominant noise processes). Our method is also quite general in view that the optimised parameters are not restricted to circuit parameters: a number of generalisations can be considered in that regard, e.g., incorporating the optimisation of an active error correction [34, 35, 36], and pulse control. Our scheme could also be extended to multiparameter estimation quantum metrology.

This manuscript is organised in the following way. We begin by briefly reviewing key notions used in quantum metrology in Sec. 2. We then introduce the main idea of using variational algorithms for quantum metrology in Sec. 3 and numerical simulations of these algorithms are outlined in Sec. 4. Our main results on finding error-robust quantum states are contained in Sec. 5. We finally outline an experimental setup of our algorithm that could potentially be implemented on near-term hardware.

## 2. Precision in quantum metrology

We briefly recall basic notions used in quantum metrology in this section. We refer to reviews as, e.g., [12, 13], for more details.

Assume that the task is, e.g., to measure an external magnetic field by using an initially prepared probe state  $|\psi\rangle$  of  $N$  qubits. In this case the Hamiltonian in units of  $\hbar = 1$  is proportional to the collective angular momentum component  $J_z$  as

$$\mathcal{H} := \omega J_z = \omega \sum_{k=1}^N \sigma_z^{(k)},$$

where  $\sigma_z^{(k)}$  is the Pauli  $Z$  operator acting on qubit  $k$ , and  $\omega$  is the field strength to be probed. If there are no imperfections, the time evolution of an initially prepared probe state is described by the unitary operator  $U(\omega t) = \exp(-it\omega J_z)$  that generates

a global rotation of all qubits. One can subsequently perform projective measurements on identically prepared copies of  $|\psi(\omega t)\rangle := U(\omega t)|\psi\rangle$  and results of these measurements can be used to estimate the parameter  $\omega$ . Note that if we take into account the effect of noise on the system during the evolution period, the state to be measured is described by a density matrix  $\rho_\omega$ .

Let us assume that the measurement is described simply by an observable  $O$  which decomposes into the projectors

$$O = \sum_{n=1}^d \lambda_n |n\rangle\langle n| \quad (1)$$

with  $d = 2^N$  and the expectation values of these projectors define the probabilities of measurement outcomes  $p(n|\omega) := \text{tr}[\rho_\omega |n\rangle\langle n|]$  that depend on the parameter  $\omega$  ‡.

Measurements performed on  $\nu$  identical copies of the state at a fixed  $\omega$  can be used to estimate the value of  $\omega$  via, e.g., a maximum likelihood estimator [13, 14, 12]. The likelihood function tends to a Gaussian distribution [13, 14, 12] for an increasing number of independent measurements  $\nu$  that is centred at the true value  $\omega$  and its inverse variance  $\sigma^{-2}$  asymptotically approaches the classical Fisher information  $\nu F_c(O)$ , which we will refer to as the precision. In general, the estimation error  $\Delta\omega$  of the parameter  $\omega$  is bounded by the so-called Cramér-Rao bound

$$\Delta\omega \geq (\Delta\omega)_{\text{CR}} := [\nu F_c(O)]^{-1/2}, \quad (2)$$

where  $F_c(O)$  is the classical Fisher information of the probability distribution  $p(n|\omega)$  that corresponds to eigenstates of the observable  $O$  from Eq. (1) and  $\nu$  is the number of independent measurements. The explicit form of the classical Fisher information can be specified in terms of the measurement probabilities as

$$F_c(O) = \sum_n p(n|\omega) \left( \frac{\partial \ln p(n|\omega)}{\partial \omega} \right)^2.$$

The best possible estimation error using a fixed probe state can be obtained by maximising Eq. 2 over all possible generalised measurements [45, 46, 13, 14, 12] which leads to the so-called quantum Cramér-Rao bound

$$(\Delta\omega)_{\text{CR}} \geq (\Delta\omega)_{\text{max}} := [\nu F_Q(\rho_\omega)]^{-1/2}, \quad (3)$$

where  $F_Q(\rho_\omega)$  is the so-called quantum Fisher information of the state  $\rho_\omega$  [45, 46, 13, 14, 12].

This quantum Fisher information can be calculated for an arbitrary state  $\rho_\omega$  via the expectation value  $F_Q(\rho_\omega) = \text{tr}[\rho_\omega L^2]$  of the Hermitian symmetric logarithmic derivative  $L$  that is defined via

$$\frac{\partial \rho_\omega}{\partial \omega} := \frac{1}{2}(L\rho_\omega + \rho_\omega L). \quad (4)$$

This symmetric logarithmic derivative can be obtained for a density matrix by first decomposing it into  $\rho_\omega = \sum_k p_k |\psi_k\rangle\langle\psi_k|$  projectors onto its eigenstates  $|\psi_k\rangle$  with  $p_k > 0$ .

‡ Note that this simple measurement scheme generalises to POVM operators, refer to [44, 12]

Matrix elements of the symmetric logarithmic derivative can then be obtained explicitly [47, 48]

$$L_{ij} := \langle \psi_i | L | \psi_j \rangle = \frac{2}{p_i + p_j} \langle \psi_i | \frac{\partial \rho_\omega}{\partial \omega} | \psi_j \rangle. \quad (5)$$

This formula simplifies for a unitary evolution as the derivative  $\partial \rho_\omega / (\partial \omega)$  reduces to the commutator  $i[\rho_\omega, \mathcal{H}]$ . Its calculation is more involved in case if the evolution is not unitary [47, 48]. Besides calculating the quantum Fisher information, the symmetric logarithmic derivative is also useful for determining the optimal measurement basis. In particular, performing measurements in the eigenbasis of  $L$  saturates the quantum Cramér-Rao bound [12, 45].

The fidelity between two density matrices [44]

$$\text{Fid}(\rho_1, \rho_2) := (\text{tr}[\sqrt{\sqrt{\rho_1} \rho_2 \sqrt{\rho_1}}])^2$$

is also related to the quantum Fisher information. Assume that two density matrices  $\rho(\omega)$  and  $\rho(\omega + \delta_\omega)$  undergo the same noise process but one is exposed to an external field  $\omega$  while the other is exposed to  $\omega + \delta_\omega$ . The quantum Fisher information in this case [12] is recovered via the limit

$$F_Q[\rho(\omega)] = 8 \lim_{\delta_\omega \rightarrow 0} \frac{1 - \text{Fid}[\rho(\omega), \rho(\omega + \delta_\omega)]}{(\delta_\omega)^2}. \quad (6)$$

### 3. Variational state preparation for metrology

We consider a hypothetical device that is depicted in Fig. 2 and which first initialises a system of  $N$  qubits in the computational 0 state. Its parametrised encoder circuit then creates a probe state that is exposed to the external field whose parameter  $\omega$  is estimated. The resulting state is finally analysed to obtain an estimate of  $\omega$ .

Let us assume that an optimal probe state  $|\psi_{\text{opt}}\rangle$  maximises the metrological performance under a particular environmental noise model and experimental imperfections during the sensing period. We aim to *approximate* this optimal state with a parametrised probe state  $|\psi(\underline{\theta}_{\text{opt}})\rangle \approx |\psi_{\text{opt}}\rangle$  that is prepared via a shallow ansatz circuit  $|\psi(\underline{\theta})\rangle := U_E(\underline{\theta})|\psi_0\rangle$  which acts on the computational 0 state  $|\psi_0\rangle := |0 \dots 00\rangle$  of  $N$  qubits. We assume for simplicity that this ansatz circuit is unitary and it decomposes into single and two-qubit quantum gates

$$U_E(\underline{\theta}) := U_\mu(\theta_\mu) \dots U_2(\theta_2) U_1(\theta_1), \quad (7)$$

each of which depends on a parameter  $\theta_i$  with  $i = \{1, 2, \dots, \mu\}$ . This parametrisation  $\underline{\theta}$  corresponds to rotation angles of single and two-qubit quantum gates and it is externally optimised to find  $\underline{\theta}_{\text{opt}}$ . We propose an explicit ansatz construction for the encoder as a shallow quantum circuit that depends on a classically tractable number of parameters in Sec. 5.1 and find that it can well approximate optimal states for various environmental noise models.

After preparing the ansatz state  $|\psi(\underline{\theta})\rangle$  at a given set of parameters  $\underline{\theta}$ , it is exposed to the environment. This process is characterised by a mapping  $\Phi_{\omega t}(\cdot)$  of density matrices

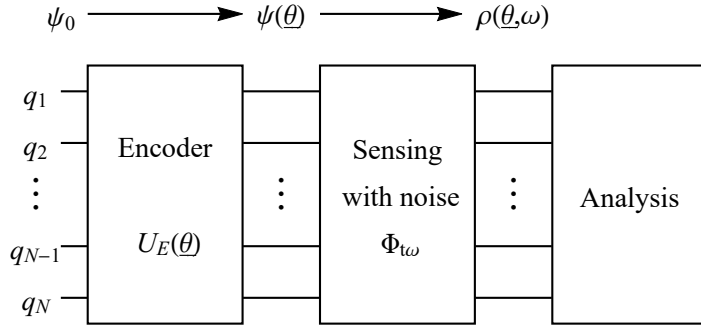


**Figure 2.** Circuit that potentially finds the quantum state  $\psi(\underline{\theta})$  that gives the best precision when estimating the parameter as the external field strength  $\omega$ .

that models the evolution under both the external field and under a non-unitary noise process, and depends on both time  $t$  and the parameter  $\omega$ . We assume that this process is continuous in time. Adapting results on infinitesimal divisible channels [49, 50], we define the explicit action of this process on any density matrix  $\rho$  via

$$\Phi_{\omega t}(\rho) = e^{-i\omega t \mathcal{J}_z + \gamma t \mathcal{L}} \rho, \quad (8)$$

where  $\omega \mathcal{J}_z$  is the superoperator representation of the external field Hamiltonian  $\omega J_z := \omega \sum_{k=1}^N \sigma_z^{(k)}/2$  which generates unitary dynamics  $\mathcal{J}_z \rho := [J_z, \rho]$  and the parameter  $\omega$  is to be estimated. The superoperator  $\mathcal{L}$  generates non-unitary dynamics via a completely positive trace preserving map between density operators and  $\gamma$  is the decay rate of the error model that can, in certain cases, depend on time  $\S$ . Note that this form is very general and independent of the particular choice of the noise model (as long as the process is continuous in time), and goes beyond previous investigations on quantum metrology [37, 38, 39] that used noise models that commute with the external field evolution.

After exposing  $|\psi(\underline{\theta})\rangle$  to the field, we denote its mixed state by the density matrix  $\rho(\omega t, \underline{\theta})$ . This state contains information about the external field, which information is deteriorated by noise during the evolution time  $t$ . The information about the evolution can be read out during the analysis period. By repeating the experiment  $\nu$  times, the estimation precision of the parameter  $\omega$  can be increased. And this precision depends on the amount of information about  $\omega$  contained in the state  $\rho(\omega t, \underline{\theta})$  and can be quantified using the quantum Fisher information. We aim to maximise this estimation precision by simultaneously varying the encoder parameters  $\underline{\theta}$  and the exposure time  $t$  that the probe state spends in the noisy environment. We thereby aim to simultaneously maximise the information about the external field  $\omega$  while minimising the effect of noise on the probe state. This will result in states  $|\psi(\underline{\theta})\rangle$  that are (near)optimally sensitive to the external field while being robust to noise. We numerically simulate this procedure in Sec. 4 and

$\S$  In this work we consider a straightforward generalisation of Eq. (8) by allowing time-dependent decay rates as well  $\gamma t \rightarrow f(t)$ . These processes belong to the most general class of continuous channels, called infinitesimal divisible channels [49, 50]

obtain (near) optimal states for metrology using the estimation precision of  $\omega$  as a target function while details of an experimental implementation of our procedure have been deferred to Sec. 6. This experimental implementation has an explicit construction of the analysis step and does not rely on the quantum Fisher information.

#### 4. Numerical simulations

We numerically (exactly) simulate the device introduced in the previous section using the software package QuEST which can efficiently simulate quantum circuits including noise processes [51]. We assume that the only source of error is the evolution under the external field due to the process  $\Phi_{\omega t}(\cdot)$  and that the encoder and analysis steps are perfect and require negligible time compared to the sensing time  $t$ . These are considerably good approximations since the optimal sensing time  $t$  is proportional to the coherence time  $1/\gamma$  (see below). This optimal time results in a significant buildup of error during the sensing period independently of the decay rate  $\gamma$  as also expected from, e.g., [23, 37]. Moreover, the sensing time is significantly longer than the time required by the encoder circuit and we assume the condition  $\gamma t_{\text{enc}} \ll 1$ , where  $t_{\text{enc}}$  is the time required for state preparation. We remark that even if preparation is negligibly short, experimental imperfections of current and near-term hardware, such as imperfections in quantum gates or measurement errors, might result in imperfect mixed probe states and measurements. We model gate imperfections in Appendix D using state-of-the-art noise rates and demonstrate that the advantage of our approach is still attainable when assuming imperfect preparation circuits. We additionally assume that each experiment can be repeated  $\nu = T/t$  times, where  $T$  is the overall time of the metrology task.

We simulate a variety of encoder circuits that generate, e.g., GHZ, classical product and squeezed states or arbitrary symmetric states. These states are introduced in more detail in Sec. 5.1. After initialising the parametrised sensing state  $|\psi(\underline{\theta})\rangle$ , the evolution under the external field is modelled using a Kraus-map representation of the process  $\Phi_{\omega t}(\cdot)$  introduced in Eq. (8). QuEST allows for modeling arbitrary one and two-qubit errors [51] via their Kraus map representations and we simulate various different error models in Sec. 5.3 including, e.g., dephasing, amplitude damping and inhomogeneous Pauli errors.

The resulting density matrix  $\rho(\omega t, \underline{\theta})$  could be used to estimate the parameter  $\omega$ . As established in Sec. 2, the performance of this task is completely determined by the quantum Fisher information  $F_Q[\rho(\omega t, \underline{\theta})]$  of this density matrix. Note that numerically calculating the quantum Fisher information of  $\rho(\omega t, \underline{\theta})$  avoids simulating the analysis step, however, it is completely equivalent to that. We remark that explicit expressions are readily available in the literature [47, 48] for computing the quantum Fisher information from the eigendecomposition of the density matrix. However, these formulas require the knowledge of the derivative  $\partial_\omega \rho(\omega)$  (or derivatives of eigenvalues and eigenvectors of  $\rho$ ) which one might only be able to compute approximately using, e.g., a finite difference approach in  $\omega$  – as in our explicit noise simulations using



QuEST. A finite difference in Eq. 6 might provide a numerically more stable and more efficient approximation than the aforementioned eigendecomposition of the approximate derivative of the density operator.

We calculate this quantum Fisher information and the resulting precision by evaluating the circuit at two different evolutions. Note that for noise channels which commute with the external field (see Sec. 5.3) the quantum Fisher information does not depend on the actual value of the parameter  $\omega$ . However, in general the choice  $\omega \rightarrow 0$  is adequate only when the field to be sensed is sufficiently small. Nevertheless, we expect that most experimentally relevant environmental noise models approximately commute with the external field evolution as discussed in Sec 5.3. In our simulations we assume the density matrices  $\rho_0 := \Phi_0(|\psi(\underline{\theta})\rangle)$  and  $\rho_1 := \Phi_{\delta_\omega t}(|\psi(\underline{\theta})\rangle)$  via setting the parameter in Eq. (8) as  $\omega \rightarrow 0$  and  $\omega \rightarrow \delta_\omega$ , respectively, and  $\delta_\omega t \ll 1$ . We then approximate the precision via the fidelity

$$(\Delta\omega)_{\max}^{-2} = \frac{T}{t} F_Q[\rho_0] = 8T \frac{1 - \text{Fid}(\rho_0, \rho_1)}{t(\delta_\omega)^2} + \mathcal{O}(\delta_\omega). \quad (9)$$

Here we assume that the experiment can be repeated  $\nu = T/t$  times, where  $t$  is the sensing time (approximately the overall time of executing the circuit once) and  $T$  is a constant (overall time of the metrology task). Note that the decay rate  $\gamma$  from Eq. (8) is a parameter that can be set freely in the simulations, however, the product  $\gamma/T(\Delta\omega)_{\max}^{-2}$  is dimensionless and independent of both  $\gamma$  and  $T$ , refer to Appendix A and also to [37]. We simulate metrology experiments with arbitrarily fixed  $\gamma \gg \delta_\omega$  and optimise the dimensionless precision  $\gamma/T(\Delta\omega)_{\max}^{-2}$  over the parameters  $\underline{\theta}$  and  $t$ . We finally obtain states that are (near) optimal for metrology in the presence of noise.

## 5. Results

### 5.1. Probe states

We simulate a variety of encoder circuits, but we do not aim to directly search in the full, exponentially large state space of  $N$  qubits. Note that this problem would require encoder circuits that correspond to arbitrary unitary transformations and would generally require exponentially many, i.e., at least  $2^N$ , parameters to be optimised. Instead, we employ circuits that contain a constant or linear number of parameters in the number of qubits which can still sufficiently well approximate the optimal probe states  $|\psi(\underline{\theta})\rangle$ . We also consider special cases of the general encoder circuit that generate, e.g., a family of squeezed states or GHZ states, in order to compare our results to previously known states for metrology.

Results of the optimisations are shown in Fig. 4 for various error models and probe states. In particular, probe states include GHZ (Fig. 4 red) and classical states (Fig. 4 black) that we define as

$$|\text{GHZ}\rangle := \frac{1}{\sqrt{2}}|0\rangle^{\otimes N} + e^{-i\phi} \frac{1}{\sqrt{2}}|1\rangle^{\otimes N}, \quad (10)$$

$$|+\dots\rangle := \left[ \frac{1}{\sqrt{2}}|0\rangle + e^{-i\phi} \frac{1}{\sqrt{2}}|1\rangle \right]^{\otimes N}, \quad (11)$$

and their only parameters that we optimise are the phase angles  $\underline{\theta} = \phi$ . Optimising these phase angles improves the metrological performance in the case when noise is not rotationally symmetric around the external field Hamiltonian, e.g., in the case of inhomogeneous Pauli errors. We remark that GHZ states can be prepared using shallow circuits consisting of a ladder of  $N - 1$  CNOT gates applied to the state  $|+\rangle \otimes |0\rangle^{\otimes(N-1)}$ .

One axis twisted squeezed states (Fig. 4 grey) are obtained [52] by the interaction under the permutation symmetric Hamiltonian  $J_z^2 = \sum_{k,l=1}^N \sigma_z^{(k)} \sigma_z^{(l)}$  and we define squeezed states via

$$|\text{sq}\rangle := e^{-i\theta_3 t J_z} e^{-i\theta_2 t J_x} e^{-i\theta_1 t J_z^2} \left[ \frac{1}{\sqrt{2}} |0\rangle + \frac{1}{\sqrt{2}} |1\rangle \right]^{\otimes N},$$

and optimise their parameters  $\underline{\theta} = (\theta_1, \theta_2, \theta_3)$ . Here  $\theta_2$  generates a global rotation around the  $x$  axis to align the squeezing angle perpendicular to the external field Hamiltonian. This unitary transformation can be represented by a quantum circuit that contains parametrised controlled- $Z$  gates and parametrised local rotations of the individual qubits [38]. Data obtained for squeezed states typically show an undulating trend in the number of qubits throughout the graphs. This trend is due to the pairwise entanglement of squeezed states [52].

Optimised symmetric states (Fig. 4 brown) are obtained by a direct search in the symmetric subspace whose dimension is linear in the number of qubits. This subspace is spanned by so-called symmetric Dicke states  $|J = N/2, m\rangle$ , where  $N$  is the number of qubits and  $J$  is the total angular momentum and its  $z$  projection is  $m$ , refer to [53, 54, 55, 56]. Every symmetric state is then a linear combination of Dicke states with complex coefficients  $c_m$

$$|\text{symm}\rangle := \sum_{m=-J}^J c_m |J = N/2, m\rangle. \quad (12)$$

We optimise these coefficients in our algorithm under the constraint that their absolute value squares sum up to 1 and  $\underline{\theta} = \{c_m\}$ . Note that all states considered so far are symmetric under permutations.

In contrast to the above introduced well-known symmetric states we aim to search in the space of general qubit states via an ansatz circuit (Fig. 4 green) that decomposes into single and two qubit gates from Eq. (7). In particular, we use a circuit shown in Fig. 3 that has a classically tractable number of parameters, i.e., linear in the number  $N$  of qubits. This ansatz structure is periodic and decomposes into repeated blocks. The first block  $B_1$  consists of  $N$  single qubit  $X$ -rotations acting on individual qubits with independent rotation angles  $\theta_i$ . The second block  $B_2$  contains  $N$  controlled- $Y$  rotations acting on nearest neighbour qubits followed by single qubit  $Z$ -rotations acting on individual qubits and all gates have independent rotation angles  $\theta_i$ . We found that the ansatz structure  $B_2 B_2 B_1 B_2 B_2 B_1$  can well approximate metrologically optimal states for a variety of noise models for  $N \leq 9$ , even though it cannot exactly reproduce arbitrary states in the exponentially large Hilbert space. Moreover, increasing the number of repeated blocks allows for better approximations of the optimal states. We additionally



*general* and there exist  $N!$  sets of parameters that correspond to the same metrological performance in an  $N$ -qubit system. This high degree of symmetry of the objective function can be exploited to speed up the search even when no assumptions about the optimal parameters are made.

### 5.3. Probe states optimised against noise

*Dephasing error* — It has been known that GHZ states perform equally well as classical product states when undergoing dephasing [23], i.e., if the only source of noise is the stochastic fluctuation of the parameter  $\omega$  during the evolution period. We simulate metrology experiments in the case when noise is dominated by dephasing. In this special case all superoperators in Eq. (8) commute and the evolution reduces to the explicit equation

$$\Phi_{\omega t}(\rho) = \left[ \prod_{k=1}^N e^{\gamma t \mathcal{L}_{\text{de}}^{(k)}} \right] e^{-i\omega t \mathcal{J}_z} \rho \quad (13)$$

which contains the superoperator  $\omega \mathcal{J}_z$  that generates the unitary evolution under the external field Hamiltonian  $\omega J_z = \omega \sum_{k=1}^N \sigma_z^{(k)}/2$  and the non-unitary dephasing superoperator  $\mathcal{L}_{\text{de}}^{(k)}$  that effects all the  $N$  qubits (indexed by  $k$ ) identically and independently. We use the Kraus map representation of the dephasing channel that acts on an individual, single qubit via

$$e^{\gamma t \mathcal{L}_{\text{de}}^{(k)}} \rho := [1 - p(t)]\rho + p(t)\sigma_z^{(k)}\rho\sigma_z^{(k)} \quad (14)$$

and we define its time-dependent probability as  $p(t) := (1 - e^{-\gamma t})/2$ . We apply this channel to the initialised probe state  $|\psi(\underline{\theta})\rangle$  and calculate the dimensionless precision via the quantum fisher information of the resulting density matrix  $\rho(\omega t, \underline{\theta})$  as discussed below Eq. (9).

Fig. 4 a) (left) shows the scaling of the dimensionless precision for a variety of different optimised probe states in case of dephasing noise. The dimensionless precision of the previously discussed GHZ and product states can be derived analytically as  $\gamma/T(\Delta\omega)_{\text{max}}^{-2} = N/(2e)$  where  $e$  is the Euler number and Fig. 4 a) (left) GHZ (red) and separable (black) states match the analytically derived formulas [23]. This precision has a classical scaling, i.e., linear in the number of qubits  $N$ . Note that all states in Fig. 4 a) (left) display a classical, linear scaling in the number of qubits which conforms with the asymptotic bounds on the quantum Fisher information obtained for usual Markovian channels [38, 39, 64, 24, 25]. In particular, an upper bound on the quantum Fisher information is saturated asymptotically by squeezed states [23, 38, 39] in case of dephasing noise. GHZ and separable states, therefore, can be outperformed by using optimised probe states but only up to an enhancement of a constant factor at most  $e \approx 2.72$  [23, 38, 39].

The dimensionless precision achieved in our simulations with squeezed states (grey) is nearly optimal and results in a comparable performance to general symmetric states (brown) and ansatz states (green) as also expected from [23, 38, 39]. Our results conform

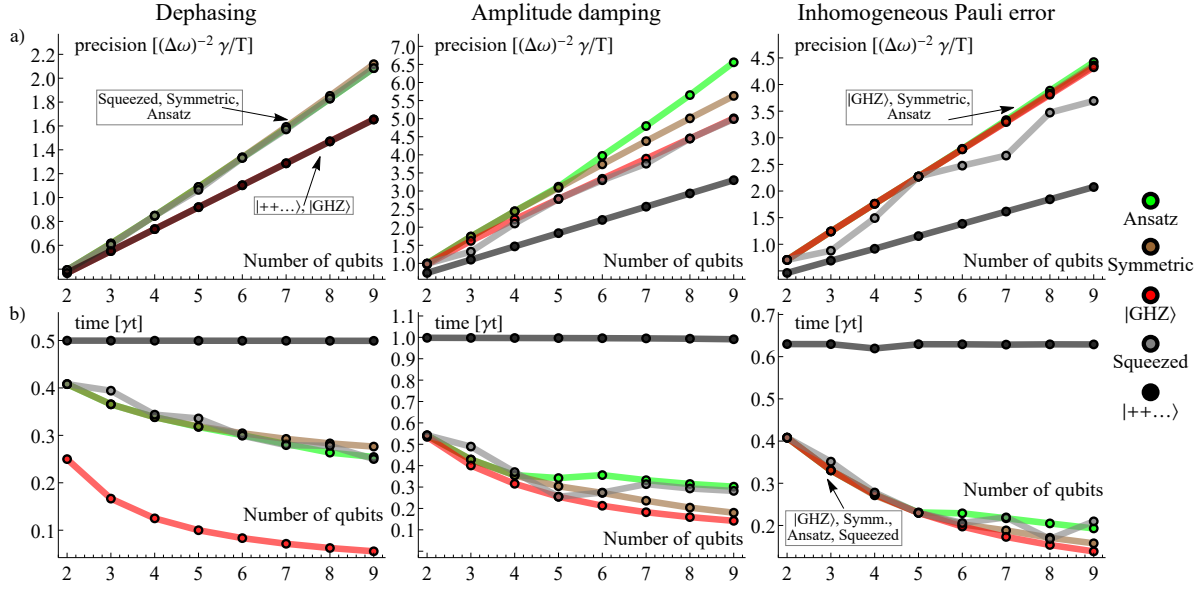


**Figure 4.** a) scaling of the optimised dimensionless precision as a function of the number of qubits calculated for a variety of probe states and noise models. Optimal ansatz states (green) obtained via the encoder circuit from Fig. 3 outperform any symmetric state (brown) and break permutation symmetry in certain, practically relevant noise models. Note that values on the  $y$  axis are independent of the actual decay rate  $\gamma$  of the noise model and independent of the overall time  $T$  of the experiment (which consists of several repeated sub-experiments) when expressed in units of  $\gamma/T$ . b) optimised probing time, i.e., optimal time that the probe state spends in the noisy environment. This time typically varies between  $\propto 1$  and  $\propto 1/N$  in units of the error model’s decay time and  $N$  is the number of qubits.

with optimisations performed in [23] for a small number of qubits using symmetric states. Note that our ansatz states (green) have a negligible difference in performance when compared to general symmetric states (brown). This difference is due to the fixed, finite depth of our ansatz circuit (which can only *approximate* arbitrary qubit states) and can be reduced by increasing the circuit depth. Most importantly, this negligible difference in performance verifies that our approach using the ansatz circuit has (approximately) found the metrologically optimal states.

Fig. 4 b) (left) shows the optimal sensing times for the various probe states. These optimal sensing times can be derived analytically for the GHZ state [23] (in units of the decay time) as  $\gamma t_{\text{opt}} = (2N)^{-1}$  and for the classical product state as  $\gamma t_{\text{opt}} = 1/2$ , where  $N$  is the number of qubits. The near-optimal squeezed (grey), symmetric (brown) and general qubit (green) states tend to spend more time than  $(2N)^{-1}$  in the noisy environment but less time than  $1/2$ .

*Amplitude damping error* — We now consider a noise process in which amplitude damping or equivalently spontaneous emission dominates. Similarly as with the dephasing channel, all terms in Eq. (8) commute and the evolution reduces to an analogous form with Eq. (13) but noise is now modelled using the damping

superoperators

$$e^{\gamma t \mathcal{L}_{\text{da}}^{(k)}} \rho := K_1^{(k)} \rho K_1^{(k)} + K_2^{(k)} \rho [K_2^{(k)}]^\dagger \quad (15)$$

that effect all qubits identically and independently. We have used here the Kraus map representation of this channel with the time-dependent Kraus operators

$$K_1 := \begin{pmatrix} 1 & 0 \\ 0 & \sqrt{1-p(t)} \end{pmatrix}, \quad K_2 := \begin{pmatrix} 0 & \sqrt{p(t)} \\ 0 & 0 \end{pmatrix},$$

and their time-dependent probability is  $p(t) := 1 - e^{-\gamma t}$ .

Fig. 4 a) (mid.) shows the scaling of the dimensionless precision for a variety of different probe states that were optimised against amplitude damping error. Note that all curves have a linear, classical scaling in the number of qubits which conforms with the linear asymptotic bound [64, 24, 25, 39] on the quantum Fisher information obtained for this noise channel. Under the amplitude damping error, GHZ states (red) perform significantly better than classical product states (black). Note that in the analysed region (2-9 qubits) squeezed states (grey) closely approach the performance of GHZ states (red). On the other hand, optimised general probe states offer significant improvements. In particular, general symmetric states (brown) have a linear scaling but a steeper slope than GHZ states. Moreover, relaxing permutation-symmetry constraints on the probe state (green) results in further improvements. Although the metrological task is permutation symmetric, i.e., its Hamiltonian and noise model is invariant under permutations, our algorithm can discover non-symmetric states that evidently outperform every symmetric state. These optimised ansatz states (green) are not permutation symmetric for  $N \geq 5$  and can apparently spend longer time in the environment. Of course, the corresponding optimal measurement basis that saturates the Cramér-Rao inequality consists of states that are not permutation symmetric either. Refer to Sec. 5.4 for a more detailed discussion of these states. Moreover, we simulate state-of-the-art noise rates in Appendix D and demonstrate that the superior performance of these non-symmetric states persists even when we take into account gate imperfections in their preparation circuits.

Fig. 4 b) (mid.) shows the optimal probing time. Optimised symmetric states (brown, grey) can spend more time in the noisy environment than GHZ states and perform better. Ansatz states (green) have no permutation symmetry [Fig. 6 b) (mid.)] for  $N \geq 5$  and can apparently spend significantly more time in the environment and this time appears to have a more preferable scaling in the number of qubits when compared to symmetric states. This advantage of ansatz states results in a significantly better performance than optimised symmetric states. Refer to Sec. 5.4 for a more detailed analysis of the resulting optimal states.

*Inhomogeneous Pauli error* — The errors considered so far were rotationally symmetric with respect to the external field and their superoperators therefore commute with the external field evolution. In the following we consider an error model that contains Pauli errors with no axial symmetry, such as bit flips. In particular, we

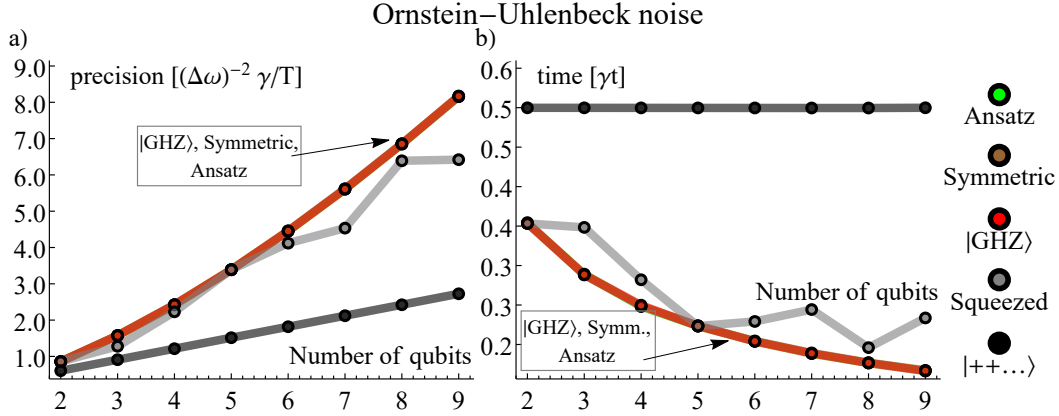


**Figure 5.** Optimised dimensionless precision a) and probing time b) for a variety of probe states in case if noise is dominated by a random fluctuation of the external field parameter  $\omega$ . We assume that this random fluctuation is described by the Ornstein-Uhlenbeck process in the limit of long correlation times, i.e., by a non-Markovian process. The zero-correlation-time limit yields dephasing from Fig. 4 (left).

explicitly define and fix the process in Eq. (8) at zero external field, i.e.,  $\omega = 0$  and at the particular time  $\gamma t = 1$  via the Kraus map

$$e^{\mathcal{L}_{\text{pa}}^{(k)}} \rho := [1 - \sum_{\alpha} p_{\alpha}] \rho + \sum_{\alpha} p_{\alpha} \sigma_{\alpha}^{(k)} \rho \sigma_{\alpha}^{(k)} \quad (16)$$

that acts on each qubit identically and individually. Here  $\alpha \in \{x, y, z\}$  and the time-dependent probabilities are asymmetric (inhomogeneous)  $2p_x = p_y = 4p_z$  and their sum is fixed to  $\frac{3}{4}(1 - e^{-1})$ . In the simulations we represent this Kraus map as a superoperator matrix [65] whose matrix logarithm then determines the generator  $\mathcal{L}_{\text{pa}}^{(k)}$ . The superoperator matrix of the entire process in Eq. (8) is calculated via the matrix exponential of the sum  $-i\omega t \sigma_z^{(k)} + \gamma t \mathcal{L}_{\text{pa}}^{(k)}$  for bounded time  $0 \leq \gamma t \leq 1$ . This time-continuous process therefore interpolates between the identity operation ( $\gamma t = 0$ ) and Eq. (16) at the particular time  $\gamma t = 1$ .

Fig. 4 a) (right) shows the optimised dimensionless precision for a variety of probe states in case of inhomogeneous Pauli errors. Note that GHZ states (red) appear to be optimal, however, optimised probe states (grey, brown, green) tend to spend more time in the environment than GHZ states for  $N \geq 6$  as shown in Fig. 4 b). This results in a slightly better performance of general symmetric states (brown). Note that similarly to the amplitude damping channel, optimal ansatz states (green) spend even longer time in the environment and outperform any symmetric state while breaking permutation-symmetry [Fig. 6 b) (right) for  $N \geq 6$ ]. Although all curves display a classical, linear scaling, it is expected that the steeper slope of ansatz states (green) results in higher improvements for an increasing system size.

*Ornstein-Uhlenbeck noise* — We finally consider a noise model that is dominated by a random fluctuation of the external field which follows the so-called Ornstein-Uhlenbeck process [66]. This noise process is non-Markovian in general and in the limit of long correlation times an improved scaling can be reached when using GHZ states as already

established by some of us in [26]. In particular, the time-dependent fluctuation of the external field is described by its zero mean  $\langle \omega'(t) \rangle = 0$  and a time-dependent correlation function [66, 67]

$$\langle \omega'(t)\omega'(\tau) \rangle = \frac{b\lambda}{2} e^{-\lambda|t-\tau|}, \quad (17)$$

where  $\langle \cdot \rangle$  denotes the expected value,  $\lambda^{-1}$  is the process' finite correlation time and  $b$  is the bandwidth of noise. This process effectively results in a time-dependent buildup of a dephasing error via the time-dependent probability  $p(t) = [1 - e^{-f(t)}]/2$  and the noise channel is described by the Kraus-map representation

$$e^{-f(t)\mathcal{L}_{\text{de}}^{(k)}} \rho := [1 - p(t)]\rho + p(t)\sigma_z^{(k)}\rho\sigma_z^{(k)}, \quad (18)$$

from Appendix B. This channel is analogous with simple dephasing from Eq. (14) up to the time-dependent decay rate  $\gamma t \rightarrow f(t)$ . This time-dependent decay rate was derived explicitly in [67] as  $f(t) := b[t + (e^{-\lambda t} - 1)/\lambda]/2$ . Note that this noise model reduces to simple dephasing from Eq. (14) in the limit of short correlation times, i.e., when  $b^{-1} \gg \lambda^{-1}$  and  $\lambda^{-1}$  is the correlation time. In this case the decay rate is characterised by  $f(t) \approx bt/2$  the bandwidth of the classical process [67].

We now consider the limit of long correlation times with  $b^{-1} \ll \lambda^{-1}$  as an example of non-Markovian channels. In this case the time-dependent decay rate reduces to  $f(t) \approx b\lambda t^2/4$  and this process is analogous to standard dephasing from Eq. (14) up to the time-dependent probabilities  $p(t) = [1 - e^{-(\gamma t)^2}]/2$  with  $\gamma = \sqrt{b\lambda}/2$ , refer also to [67, 26, 27]. Fig. 5 a) shows the optimised dimensionless precision for various probe states. Note that the classical product state can significantly be outperformed by using entangled quantum states. In particular, optimised probe states have an improved scaling, i.e., their dimensionless precision scales as  $(\Delta\omega)_{\text{max}}^{-2} \propto N^c$  in the number of qubits with  $1 < c \leq 2$  as also expected from [26, 27]. The increased, time-dependent buildup of noise forces the system to spend the shortest possible time in the environment as shown in Fig. 5 b). GHZ states are therefore optimal and have an improved scaling [26, 27]. This again confirms that our approach (approximately) finds the optimal states.

#### 5.4. Analysis of the optimal states

We analyse the optimised probe states by first calculating and plotting simple measures that quantify their entanglement in Fig. 6 a) and their permutation symmetry in Fig. 6 b). In particular, we calculate an entanglement measure  $S_{\text{avg}}(|\psi\rangle)$  of the  $N$ -qubit system via the average von Neumann entropy as

$$S_{\text{avg}}(|\psi\rangle) := \frac{1}{N} \sum_{k=1}^N -\text{tr}[\rho_k \log_2(\rho_k)],$$

where the single-qubit reduced density operator  $\rho_k$  is obtained via the partial trace of the state  $|\psi\rangle$  over all qubits except qubit number  $k$ . This quantity is related to the Mayer-Wallach measure and quantifies the average entanglement between a single qubit and the rest of the system, refer to [68, 69, 70]. Fig. 6 a) shows that classical product



states (black) are unentangled but all other optimised states are highly entangled. It has been known that optimal states in case of dephasing are less entangled than GHZ states [23, 38, 39]. Optimised general symmetric (brown) and ansatz states (green) have slightly less linear entanglement than GHZ states in case of both dephasing and amplitude damping errors Fig. 6 a) (left and mid.). These optimised states are, however, very close to a GHZ state in case of Pauli errors in Fig. 6 a) (right) and have therefore similar linear entanglement.

We quantify permutation symmetry by calculating the the average fidelity of all permutations of the state  $|\psi\rangle$

$$P_{\text{avg}}(|\psi\rangle) := \frac{1}{N_p} \sum_{k=1}^{N_p} \text{Fid}[|\psi\rangle, P_k|\psi\rangle],$$

where  $P_k$  permutes two qubits and  $k$  runs over all distinct permutations with  $N_p = \binom{N}{2}$ . Fig. 6 b) shows that all symmetric probe states have a maximal permutation symmetry and only ansatz states (green) can relax this symmetry. Optimal ansatz states Fig. 6 b) (green) clearly show a broken permutation symmetry in case of amplitude damping and inhomogeneous Pauli errors (mid. and right) which results in a superior performance when compared to symmetric states. Relaxing permutation symmetry offers a significant improvement of the metrological sensitivity when noise is dominated by amplitude damping, c.f. green and brown lines in Fig. 4 a) (mid.). Based on numerical evidence, we conjecture that in the case of an even number of qubits the states  $|\psi_a\rangle$  are near-optimal against amplitude damping with suitable  $c_1, c_2, c_3 \in \mathbb{C}$

$$|\psi_a\rangle := c_1|11 \cdots 1\rangle + c_2|D\rangle + c_3|00 \cdots 0\rangle, \quad (19)$$

while the component  $|D\rangle$  breaks permutation symmetry and decomposes into the computational basis states

$$\sqrt{\frac{2}{N}}(|1100 \cdots 000\rangle + |0011 \cdots 000\rangle \cdots + |0000 \cdots 011\rangle).$$

This additional component  $|D\rangle$  in the state vector allows for individually resolving first-order effects of the amplitude damping channel (i.e., flips of single qubits) and results in an improved performance when compared to its symmetric counterpart, the Dicke state  $|J, J-2\rangle$  that decomposes into all permutations of a double excitation with  $J = N/2$ . For example, in case of 8 qubits the explicit value of these coefficients is  $c_1 \approx 0.77$ ,  $c_2 \approx 0.55$  and  $c_3 \approx 0.33$  while the resulting metrological performance is close to 0.3% better than what we obtained with the optimised ansatz circuit – which can only approximate the state in Eq. (19). Refer to Appendix C for a fuller analysis of the superior power of these non-symmetric states.

Symmetric states (brown) in Fig. 4 and in Fig. 5 are optimal in some error models (as in case of dephasing) and we analyse these states separately. In particular, these state are linear combinations of Dicke states from Eq. (12) and probabilities of their optimised coefficients  $c_m$  as  $|c_m|^2$  are shown for  $N = 9$  qubits in Fig. 7 b). Moreover,

|| and this measure can straightforwardly be generalised to mixed states as well

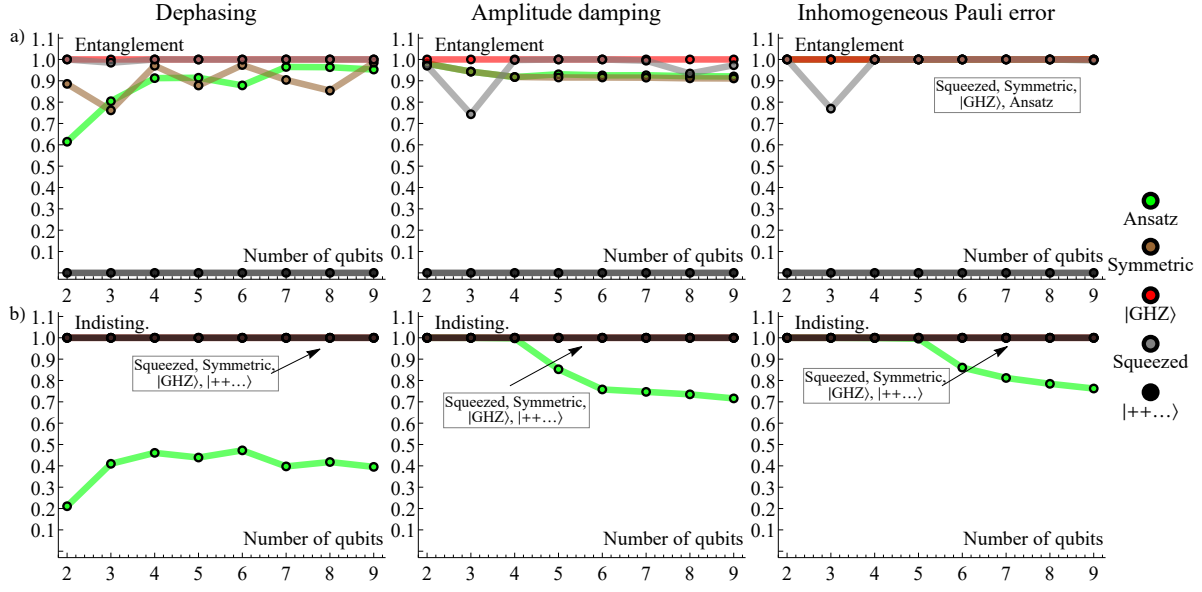


**Figure 6.** a) Linear entanglement of the optimised probe states which quantifies the average entanglement between a single qubit and the rest of the system, i.e.,  $N - 1$  qubits. b) average indistinguishability of the qubits that form the optimal probe state. Only ansatz states can relax permutation symmetry, i.e., all other states can be expressed as linear combinations of Dicke states from Eq. (12). Relaxing this symmetry offers an improved metrological sensitivity of the optimised states, see Fig. 4.

phase-space representations as the Wigner function offer an intuitive way for visualising these permutation symmetric states. The Wigner function of an arbitrary mixed state is defined as the expectation value

$$W_\rho(\Omega) = \text{Tr} [\rho \mathcal{R}(\Omega) \Pi_0 \mathcal{R}^\dagger(\Omega)] \quad (20)$$

of a rotated parity operator  $\Pi_0$  where phase space is spanned by the rotation angles  $\Omega := (\theta, \phi)$  on the sphere and  $\mathcal{R}(\Omega)$  is the rotation operator  $\mathcal{R}(\Omega) := e^{i\phi \mathcal{J}_z} e^{i\theta \mathcal{J}_y}$ , refer to [71, 72, 73, 74, 75, 76] and to works [77, 78, 79] on rotated parity operators. Fig. 7 a) shows Wigner functions of the optimal symmetric states in case of  $N = 9$  qubits.

It has been known that squeezed states are optimal asymptotically in case of dephasing [23, 38, 39]. In our simulations, squeezed states are nearly optimal in case of dephasing and Fig. 7 a) (left) shows typical characteristics of spin (over)squeezed states. In particular, a squeezed Gaussian-like distribution is surrounded by interference fringes. Moreover, Fig. 7 b) (left) identifies state-vector coefficients that are related to squeezed states as the optimal symmetric state consist of a superposition of all Dicke states with a distribution of probabilities peaked at  $m = 0$ .

GHZ states are optimal in case of the Ornstein-Uhlenbeck process and Fig. 7 a) (right) clearly identifies the Wigner function of GHZ states while Fig. 7 b) (right) shows an equal superposition of the spin-up and down states.

Symmetric states are suboptimal in case of amplitude damping and the best symmetric state is similar to a GHZ state. In particular, it is a linear combination

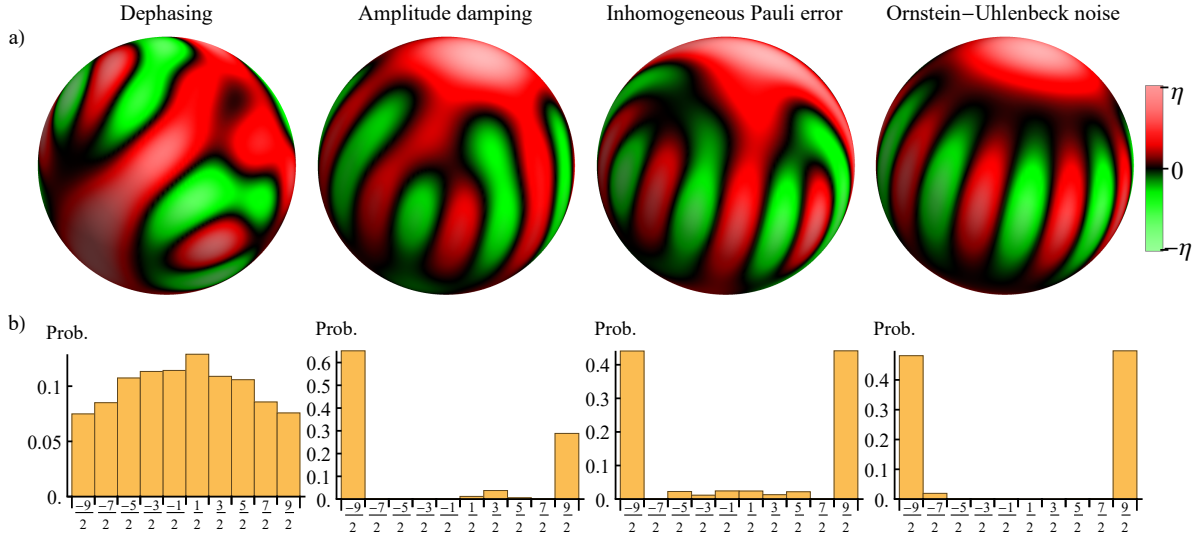


**Figure 7.** a) Wigner functions of *permutation symmetric* 9-qubit states optimised against different error models from Fig. 4 a) (brown). The Wigner function in case of dephasing is similar to a squeezed state and in case of the Ornstein-Uhlenbeck process it is very close to a GHZ state. Wigner functions in case of amplitude damping and inhomogeneous Pauli errors are related to GHZ states. Red and green colours show positive and negative values of the function while brightness represents the absolute value of the function relative to its its global maximum  $\eta$ . b) Probabilities of Dicke states with  $-9/2 \leq m \leq 9/2$  as absolute value squares of their optimised state-coefficients from Eq. (12).

of the spin-up and down states as shown in Fig. 7 b) (mid. left) but the state has a higher probability of being in the spin-down state. Its Wigner function Fig. 7 a) (mid. left) is similar to Fig. 7 a) (right).

GHZ states are nearly optimal in case of inhomogeneous Pauli errors and Fig. 7 a) (mid. right) shows a Wigner function that is similar to Fig. 7 a) (right).

## 6. Possible experimental implementation

We now outline a possible experimental setup of our approach that can be implemented on near-term hardware. In particular, we consider a hypothetical device depicted in Fig. 8 which has a set of parameters that can be varied externally. This device can read out the evolution information after the sensing period using a decoder circuit and a set of projective measurements. Results of  $\nu$  repeated executions of this device are used to estimate the precision of estimating  $\omega$  and parameters of the encoder and decoder circuits are variationally optimised to yield the best possible precision  $(\Delta\omega)_{\max}^{-2}$ .

Similarly as in Sec. 3, a probe state  $|\psi(\underline{\theta})\rangle$  is initialised using an encoder circuit and this state is then exposed to the noisy environment with the field to be probed. The resulting mixed state  $\rho(\omega t, \underline{\theta})$  is now analysed using the combination of a decoder circuit and a set of projective measurements in the computational basis. In particular, a decoding circuit is applied to the state  $\rho(\omega t, \underline{\theta})$  that converts the evolution information

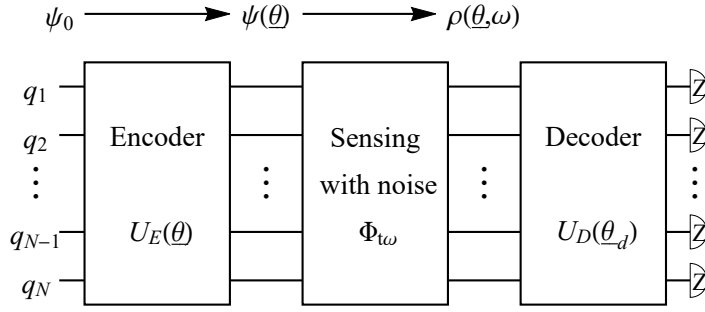


**Figure 8.** Circuit that potentially finds the quantum state  $\psi(\underline{\theta})$  that gives the best precision when estimating the parameter  $\omega$  from projective measurements.

$\omega t$  optimally into probabilities of measuring the classical registers  $|n\rangle$  at the end of the circuit. These classical registers are indexed using the binary numbers  $0 \leq n \leq 2^N - 1$ . The measurement probabilities are given by the expectation values

$$p(n|\omega) = \langle n | U_D \rho(\omega t, \underline{\theta}) U_D^\dagger | n \rangle \quad (21)$$

in the computational basis, i.e., in the eigenbasis of the collective Pauli  $z$  operator  $J_z := \sum_{k=1}^N \sigma_z^{(k)}$ . Note that the decoder circuit has the effect that it maps the computational basis states  $|n\rangle$  onto an arbitrary, effective basis  $U_D^\dagger |n\rangle$ , therefore mapping  $J_z$  onto an effective observable  $O(\underline{\theta}_d) := U_D^\dagger J_z U_D$ . This effective observable then depends on the decoder parameters  $\underline{\theta}_d$ .

Recall that the classical Fisher information is related to the measurement probabilities in the eigenbasis of the effective observable  $O(\underline{\theta}_d)$

$$(\Delta\omega)_{\text{CR}}^{-2} = \nu F_c[O(\underline{\theta}_d)] = \nu \sum_n p(n|\omega) \left( \frac{\partial \ln p(n|\omega)}{\partial \omega} \right)^2$$

from Eq. (2). The result of a single experiment using the above discussed setup yields a binary number  $n$ , the index of a classical register into which the state has collapsed. Repeating the experiment  $\nu \gg 1$  times at the fixed  $\omega$ , the probabilities here can be estimated from the measurement results and their derivatives can be approximated by repeating the experiment at an external field  $\omega + \delta_\omega$  and calculating a finite difference. Our device can therefore estimate the precision  $(\Delta\omega)_{\text{CR}}$  that we aim to maximise over the decoder parameters  $\underline{\theta}_d$ .

Note that this device has a set of parameters as  $\underline{\theta}$ ,  $\underline{\theta}_d$  and  $t$  that can be varied. In particular, maximising over the decoder parameters  $\underline{\theta}_d$  optimises the observable, in the eigenbasis of which the measurements are effectively performed. If the decoder and encoder circuits are universal, i.e., if  $U_E(\underline{\theta})$  and  $U_D(\underline{\theta}_d)$  span the group  $SU(2^N)$ , then this setup can in principle achieve the combination of an optimal sensing state  $|\psi_{\text{opt}}\rangle$  from Sec. 3 and the corresponding best measurement strategy.

Although the encoder and decoder circuits are not universal and not perfect in a practically relevant experimental implementation, we assume they can approximate the

precision via

$$\nu \max_{\underline{\theta}_d} F_c[O(\underline{\theta}_d)] \approx \nu F_Q[\rho(\omega t, \underline{\theta})] = (\Delta\omega)_{\max}^{-2}, \quad (22)$$

that we calculated in the simulations via the quantum Fisher information  $F_Q[\rho(\omega t, \underline{\theta})]$ . Note that the measurement process can be parallelised by executing the task on several identical copies of the device.

Superconducting qubits are known to be excellent candidates for realising both quantum computers and quantum sensors. High-fidelity quantum gate operations and projective measurements are a prerequisite for quantum computation and have been successfully demonstrated in [80, 81, 82]. On the other hand, superconducting qubits can contain a SQUID-structure, and so the applied magnetic fields can shift the resonant frequency of the superconducting qubits [83]. There have been several experimental demonstrations of using superconducting qubits as highly sensitive magnetic field sensors [20, 84]. Therefore, superconducting qubits are potentially suitable for experimentally demonstrating our proposal.

## 7. Discussion and conclusion

In this work we proposed variational quantum algorithms for finding quantum states that are optimal for quantum metrology in the presence of environmental noise. Ours is not the first study to consider a classical optimisation of quantum states; for example Ref. [85] employs a classical optimisation method to obtain metrologically useful states in case of quantum optics. This method is, however, limited to very small quantum systems, i.e., when the average photon number is smaller than two (due to the computational complexity of the problem). Moreover, this approach does not take the effect of noise into account. In the present study, we adapt state-of-the-art variational techniques to tackle metrology in the presence of noise; moreover, while the results we present so far have been obtained via classical simulations (using the QuEST system) our technique can be operated on real quantum hardware in order to explore beyond the classical reach. Moreover, we provide an openly available MATHEMATICA notebook in [63] that contains our simulation code using QuEST and which can be used to reproduce optimisation results contained in this manuscript as in Fig. 4.

Our study has comprehensively explored systems consisting of up to 9 qubits: we have numerically simulated experiments in case of various different error models using the same ansatz-circuit structure. We have demonstrated that our variational approach using this fixed ansatz circuit is able to find previously known optimal states despite vast differences in the error models. Moreover, we found families of (near) optimal quantum states that non-trivially outperform previously known symmetric states. In particular, we demonstrated that relaxing permutation symmetry of the probe states offers significant improvements beyond symmetric states. And we note that only these latter symmetric states have been studied in detail so far in the context of quantum metrology [23, 38, 39, 40, 41, 42, 43, 14, 12]. We remark that verifying *global* optimality

of the symmetry-breaking states is beyond the scope of the current work (although our numerical simulations did (approximately) find the optimal states in case of the non-symmetry breaking noise channels).

We analysed the resulting optimal states and found that they are usually highly entangled but not necessarily maximally entangled as can also be expected from [23]. We outlined a possible experimental realisation that could be implemented on near-term quantum hardware.

A number of natural extensions are apparent: we mention two examples here. Firstly, the approach here can be extended to consider the case that the hardware used to prepare the metrology state is itself noisy; our technique would then optimally use such hardware, with-or-without the use of error mitigation techniques. Secondly, it would clearly be interesting to combine the optimisation techniques mentioned here with the error-detecting and error-correcting concepts described in, for example, Refs. [28, 29, 30, 31, 32, 33, 34, 35, 36].

## Acknowledgments

S.C.B. acknowledges financial support from the NQIT UK National Hub, EPSRC grant EP/M013243/1. B.K. and S.C.B. acknowledge funding received from EU H2020-FETFLAG-03-2018 under the grant agreement No 820495 (AQTION). S.E. acknowledges financial support from the Japan Student Services Organization (JASSO) Student Exchange Support Program (Graduate Scholarship for Degree Seeking Students). T.J. thanks the Clarendon Fund for their continued support. Y.M. was supported by Leading Initiative for Excellent Young Researchers MEXT Japan, and was also supported by MEXT KAKENHI (Grant No. 15H05870). B.K and S.E contributed to this work equally. The authors are thankful to P. Zoller, P. Silvi and R. Kaubruegger for useful comments and their hospitality.

## Appendix A. Deriving the dimensionless precision

Recall that the precision is calculated using Eq. (6) via the fidelity

$$(\Delta\omega)_{\max}^{-2} = \frac{T}{t} F_Q[\rho_0] = 8T \frac{1 - \text{Fid}(\rho_0, \rho_1)}{t(\delta_\omega)^2} + \mathcal{O}(\delta_\omega),$$

between the density matrices  $\rho_0$  and  $\rho_1$ . In particular, the evolution process from Eq. (8) is set to  $\omega \rightarrow 0$  for  $\rho_0 := \Phi_0(|\psi(\underline{\theta})\rangle)$  and to  $\omega \rightarrow \delta_\omega$  and  $\rho_1 := \Phi_{\delta_\omega t}(|\psi(\underline{\theta})\rangle)$  which results in the explicit form

$$\begin{aligned} \rho_0 &= e^{\gamma t \mathcal{L}} |\psi(\underline{\theta})\rangle \langle \psi(\underline{\theta})|, \\ \rho_1 &= e^{-i\delta_\omega t \mathcal{J}_z + \gamma t \mathcal{L}} |\psi(\underline{\theta})\rangle \langle \psi(\underline{\theta})|, \end{aligned}$$

where  $|\psi(\underline{\theta})\rangle$  is the probe state and  $\mathcal{J}_z$ ,  $\mathcal{L}$  are superoperators. Let us now apply the transformation  $t \rightarrow t'/\gamma$  and  $\delta_\omega \rightarrow \delta'_\omega \gamma$ . Note that this transformation does not effect

the unitary evolution, i.e.,  $\delta_\omega t = \delta'_\omega t'$ , and results in the density matrices

$$\begin{aligned}\rho'_0 &= e^{t'\mathcal{L}}|\psi(\underline{\theta})\rangle\langle\psi(\underline{\theta})|, \\ \rho'_1 &= e^{-i\delta'_\omega t'\mathcal{J}_z + t'\mathcal{L}}|\psi(\underline{\theta})\rangle\langle\psi(\underline{\theta})|,\end{aligned}$$

which corresponds to the original dynamics but with effectively using a unit decay rate  $\gamma \rightarrow 1$ . The resulting precision therefore depends trivially on the parameter  $\gamma$

$$(\Delta\omega)_{\max}^{-2} = 8T \frac{1 - \text{Fid}(\rho'_0, \rho'_1)}{\gamma t' (\delta'_\omega)^2} + \mathcal{O}(\delta'_\omega).$$

The precision is therefore a function  $(\Delta\omega)_{\max}^{-2} = f(\gamma)$  of the decay rate with  $f(\gamma) = c/\gamma$  and the only degree of freedom is the constant factor  $c$ . We finally obtain the dimensionless precision  $\gamma/T(\Delta\omega)_{\max}^{-2}$  that is independent of the decay rate of our noise model.

## Appendix B. Kraus operators of the Ornstein-Uhlenbeck noise

The Kraus representation of the Ornstein-Uhlenbeck noise has been derived in [67] as in terms of the single-qubit Kraus operators

$$K_1(t) := \begin{pmatrix} q(t) & 0 \\ 0 & 1 \end{pmatrix}, \quad K_2(t) := \begin{pmatrix} \sqrt{1 - q^2(t)} & 0 \\ 0 & 0 \end{pmatrix},$$

with the time-dependent probability  $q(t) = e^{-f(t)}$  and  $f(t) := \gamma[t + (e^{-\lambda t} - 1)/\lambda]/2$ . It can be shown by a direct calculation that this Kraus map is equivalent to simple dephasing

$$K_1(t)\rho K_1(t) + K_2(t)\rho K_2(t) = [1 - p(t)]\rho + p(t)\sigma_z^{(k)}\rho\sigma_z^{(k)}$$

up to the time-dependent probability of dephasing  $p(t) = [1 - e^{-f(t)}]/2$ .

## Appendix C. Improved performance of non-symmetric states

Let us define the Dicke states  $|J, J\rangle := |00 \cdots 0\rangle$  and  $|J, -J\rangle := |11 \cdots 1\rangle$  with  $J = N/2$  for an even number of qubits  $N$ . By analysing the optimal states produced by the variational technique, i.e. the upper line in Fig. 4(mid), one can observe that for even numbers of qubits the states are close to  $|\psi_a\rangle$  given by

$$|\psi_a\rangle := c_1|J, J\rangle + c_2|D\rangle + c_3|J, -J\rangle,$$

where the component  $|D\rangle$  breaks permutation symmetry and its explicit form is

$$\sqrt{\frac{2}{N}}(|1100 \cdots 000\rangle + |0011 \cdots 000\rangle \cdots + |0000 \cdots 011\rangle).$$

For  $N = 6$  and  $N = 8$  the performance of  $|\psi_a\rangle$  almost exactly coincides with that of the variationally-determined states. In the following, we compare the states  $|\psi_a\rangle$  to their symmetric analogues

$$|\psi_s\rangle := c_1|J, J\rangle + c_2|J, J - 2\rangle + c_3|J, -J\rangle.$$

The latter under-perform the former, symmetry-broken states by a considerable margin (see Fig. 4(mid)) but are nearly optimal *within* the restriction to symmetric states (performance  $> 99\%$  of the optimal symmetric state for  $N = 8$ ). Here the Dicke state  $|J, J - 2\rangle$  contains all distinct  $\binom{N}{2}$  permutations of a double excitation.

In the following, we provide an analysis into the reason that these non-symmetric states have superior performance. Roughly speaking, the explanation is that the basis of meaningful measurements is larger, with measurements corresponding to specific first-order decay events. This increased basis leads to a correspondingly greater Fisher information.

After exposing these states to the noisy environment, their density matrices  $\rho_a$  and  $\rho_s$  contain information about the external field. This information is extracted by applying a decoder circuit to these states and performing measurements in the computational basis. The decoder circuit acts as, e.g.,  $U_d\rho_a(U_d)^\dagger$  and the probability of measuring a computational basis state  $|n\rangle$  is given by the expectation value  $\langle n|U_d\rho_a(U_d)^\dagger|n\rangle$ . This probability can be formally written as measuring in an alternative basis  $|n'\rangle = (U_d)^\dagger|n\rangle$  without the application of a decoder circuit and the equivalent probability is then given by  $\langle n'|\rho_a|n'\rangle$ . We will refer to it as the optimal measurement basis.

If there is no noise present (i.e.,  $\gamma = 0$ ) the optimal decoder circuit results for both  $\rho_a$  and  $\rho_s$  in the optimal measurement basis as  $b_1|J, J\rangle \pm b_2|J, -J\rangle$  with  $b_1 = e^{i\pi/2}b_2 = 1/\sqrt{2}$  and all other basis states are found with exactly 0 probability ¶. In the case of finite noise (i.e.,  $\gamma > 0$ )  $T_1$  relaxation events will occur but only to individual qubits in the first order. This can be shown by decomposing the Kraus operators of the amplitude damping channel into an identity operation plus  $T_1$  and  $T_2$  relaxation terms. In particular, the operator  $T_+ := |0\rangle\langle 1|$  is denoted as  $T_+^{(j)}$  when acting on qubit  $j$  and results in, e.g.,  $T_+^{(1)}|111\dots\rangle = |011\dots\rangle$ . These events will result in non-zero probabilities of additional measurement results. In particular, the optimal measurement basis of the symmetric case  $\rho_s$  will include the basis  $|S\rangle := b_1|J, J - 1\rangle \pm b_2|J, -J + 1\rangle$  which has a non-zero probability  $\text{prob}(S) := \langle S|\rho_s|S\rangle$  only because of the first-order effect of  $T_1$  relaxation.

In case of the non-symmetric state  $\rho_a$ , the optimal measurement basis includes all  $2N$  bases

$$|A_j\rangle := T_+^{(j)}(b_1|J, -J\rangle \pm b_2\sqrt{N/2}|D\rangle) \quad (\text{C.1})$$

which contain flips of individual qubits  $1 \leq j \leq N$  via the operator  $T_+$ . For example, flipping the first qubit yields

$$|A_1\rangle = b_1|0111\dots 111\rangle \pm b_2|0100\dots 000\rangle,$$

or flipping the second yields

$$|A_2\rangle = b_1|1011\dots 111\rangle \pm b_2|1000\dots 000\rangle,$$

¶ These states with  $|c_2| > 0$  are not optimal in the noiseless case and result in non-zero probabilities of bases that contain double excitations, but this does not effect our discussion



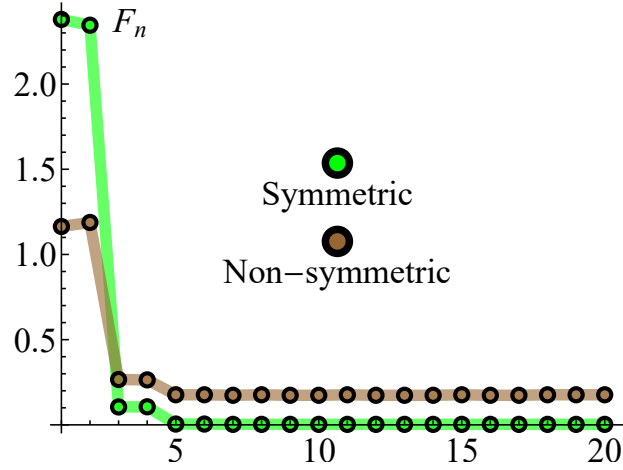


**Figure C1.** Contribution of the individual measurement bases to the classical Fisher information  $F_n$ , i.e., the sum of these individual elements results in the quantum Fisher information. (green) optimal measurement scheme with the optimised symmetric input state  $\psi_s$  and (brown) with the optimised non-symmetric input state  $\psi_a$  for  $N = 8$  qubits. The last 16 orange dots are due to measurements in the bases  $|A_j\rangle$ . The optimal symmetric state is close to a tilted GHZ state, i.e.,  $c_2 \approx 0$  and the first two green dots are therefore higher than in case of the non-symmetric scheme (brown) where  $c_2 \approx c_1$ . The optimised non-symmetric state is a trade-off between increasing the contribution  $c_2|D\rangle$  (which increases the last 16 brown dots) at the cost of decreasing the absolute value of  $c_1$  and  $c_3$  (which decreases values of the first two brown dots).

and similarly

$$|A_3\rangle = b_1|1101 \cdots 111\rangle \pm b_2|0001 \cdots 000\rangle.$$

There are overall  $2N$  of these measurement bases and their non-zero probabilities  $\langle A_j|\rho_a|A_j\rangle$  are only due to the effect of first-order  $T_1$  relaxation.

In the following, we aim to comparing the classical Fisher information due to these additional bases that extract information about the external field even after the state has undergone relaxation. In particular, its contribution to the classical Fisher information in the symmetric scenario is given by

$$F_s = \text{prob}(S)^{-1} \left( \frac{\partial \text{prob}(S)}{\partial \omega} \right)^2. \quad (\text{C.2})$$

with the probability defined as  $\text{prob}(S) := \langle S|\rho_s|S\rangle$ . Similarly for the non-symmetric case the contribution to the classical Fisher information is given by the sum

$$F_a = \sum_{j=1}^{2N} \text{prob}(A_j)^{-1} \left( \frac{\partial \text{prob}(A_j)}{\partial \omega} \right)^2 \quad (\text{C.3})$$

over all  $2N$  bases with  $\text{prob}(A_j) := \langle A_j|\rho_s|A_j\rangle$ .

In the symmetric scenario, these measurement probabilities are calculated including the effect of external field evolution as  $\text{prob}(S) = \sum_{k=1}^N |\langle S|T_+^{(k)} e^{i\omega t J_z} |\psi_s\rangle|^2$  and assuming

that a relaxation event occurred to qubit  $k$ . The overlaps can be calculated explicitly

$$\langle S|T_+^{(k)} e^{i\omega t J_z} |\psi_s\rangle = e^{i\omega t N} c_1/\sqrt{N} + e^{i\omega t 2} c_2 \frac{\sqrt{N-1}}{\sqrt{N^2/2}},$$

using the overlaps  $\langle J, -J+1|T_+^{(k)}|J, -J\rangle = 1/\sqrt{N}$  and similarly  $\langle J, J-1|T_+^{(k)}|J, J-2\rangle = (N-1)/\sqrt{N} \binom{N}{2}^{-1/2}$ .

The probabilities in the non-symmetric scenario are similarly  $\text{prob}(A_j) = \sum_{k=1}^N |\langle A_j|T_+^{(k)} e^{i\omega t J_z} |\psi_a\rangle|^2$  given by the overlaps which we calculate explicitly as

$$\langle A_j|T_+^{(k)} e^{i\omega t J_z} |\psi_a\rangle = \delta_{kj} (e^{i\omega t N} c_1 + e^{i\omega t 2} c_2/\sqrt{N/2}),$$

where  $\delta_{kj}$  is the Kronecker delta. Summing up for all qubits indexed by  $k$ , we obtain the ratio of probabilities

$$\text{prob}(S)/\text{prob}(A_j) = \mathcal{O}(N^0). \quad (\text{C.4})$$

Partial derivatives of the probabilities have a similar ratio

$$\frac{\partial \text{prob}(S)}{\partial \omega} \left[ \frac{\partial \text{prob}(A_j)}{\partial \omega} \right]^{-1} = \mathcal{O}(N^0). \quad (\text{C.5})$$

The measurement in the non-symmetric scheme is as sensitive as in the symmetric one. However, in the non-symmetric scheme there are  $N$  distinguishable measurement bases  $|A_j\rangle$ . These probabilities  $\text{prob}(A_j)$  and their derivatives determine the classical Fisher information via Eq. (C.2) and via Eq. (C.3). The increasing number of measurement bases in the non-symmetric scheme therefore results in a superior scaling  $\propto N$  of the corresponding classical Fisher information (when compared to the symmetric scenario) due to the ability of measuring in the  $2N$  distinct bases  $|A_j\rangle$ , refer to Fig. C1.

In conclusion, additional information via the above discussed scheme is extracted only from *that part* of the state to which amplitude damping occurred. It can be viewed as a correction (albeit a significant one) to the zeroth order part which both the symmetric and non-symmetric cases share. And this correction is even comparable to the zeroth order part in case of the non-symmetric scheme.

## Appendix D. Effect of non-ideal quantum circuits

We have repeated the numerical experiments of Sec. 5.3 with taking imperfections of the preparation circuits into account. We do not consider here the family of arbitrary symmetric states as those have no known efficient preparation circuits. We consider preparation circuits as discussed in Sec. 5.1 and assume that every single-qubit gate undergoes a depolarising noise with probability  $10^{-4}$  while two-qubit gates are effected by a larger depolarisation probability  $10^{-3}$ . We note that this is comparable to currently existing technology [86]. Fig. D1 (solid lines) illustrates the performance of the different families of quantum states when their preparation circuits are imperfect. Note that ansatz circuits from Sec. 5.1 are deeper than preparation circuits of GHZ states. The performance of these ansatz states therefore decrease more substantially due to gate

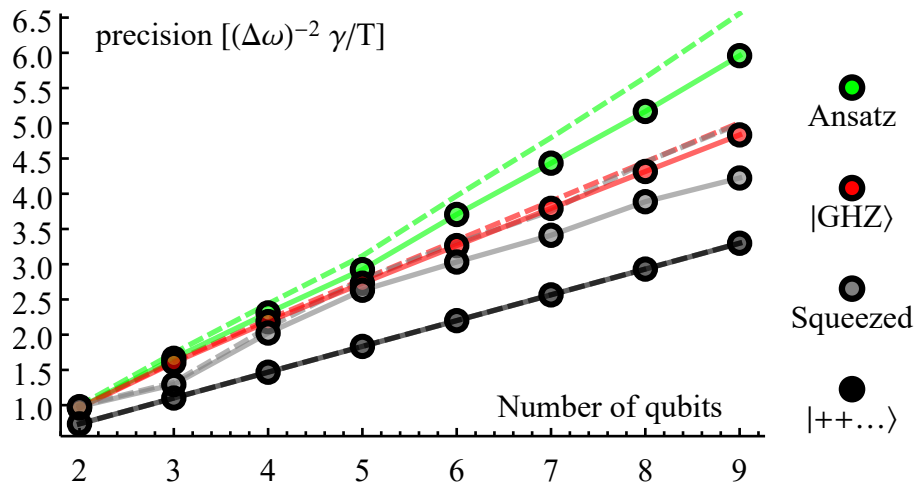


**Figure D1.** Performance of the different families of quantum states under amplitude damping when their preparation circuits are imperfect – individual gates undergo depolarising noise with a probability  $10^{-3}$  in case of two-qubit gates and  $10^{-4}$  in case of single-qubit gates. The superior performance of ansatz states over previously known ones persists despite their deeper preparation circuits. Dashed lines show the performance attained with perfect, unitary preparation circuits.

noise – compare solid to dashed lines. Nevertheless, the superior performance of ansatz states persist even under this realistic experimental noise.

## References

- [1] Alberto Peruzzo, Jarrod McClean, Peter Shadbolt, Man-Hong Yung, Xiao-Qi Zhou, Peter J Love, Alán Aspuru-Guzik, and Jeremy L Obrien. A variational eigenvalue solver on a photonic quantum processor. *Nat. Comm.*, 5:4213, 2014.
- [2] Abhinav Kandala, Antonio Mezzacapo, Kristan Temme, Maika Takita, Markus Brink, Jerry M Chow, and Jay M Gambetta. Hardware-efficient variational quantum eigensolver for small molecules and quantum magnets. *Nature*, 549(7671):242, 2017.
- [3] Nikolaj Moll, Panagiotis Barkoutsos, Lev S Bishop, Jerry M Chow, Andrew Cross, Daniel J Egger, Stefan Filipp, Andreas Fuhrer, Jay M Gambetta, Marc Ganzhorn, et al. Quantum optimization using variational algorithms on near-term quantum devices. *Quantum Sci. Technol.*, 3(3):030503, 2018.
- [4] Jarrod R McClean, Jonathan Romero, Ryan Babbush, and Alán Aspuru-Guzik. The theory of variational hybrid quantum-classical algorithms. *New J. Phys.*, 18(2):023023, 2016.
- [5] Edward Farhi, Jeffrey Goldstone, and Sam Gutmann. A quantum approximate optimization algorithm. *arXiv preprint arXiv:1411.4028*, 2014.
- [6] Ying Li and Simon C Benjamin. Efficient variational quantum simulator incorporating active error minimization. *Phys. Rev. X*, 7(2):021050, 2017.
- [7] Kosuke Mitarai, Makoto Negoro, Masahiro Kitagawa, and Keisuke Fujii. Quantum circuit learning. *Phys. Rev. A*, 98(3):032309, 2018.
- [8] Quntao Zhuang and Zheshen Zhang. Supervised Learning Enhanced by an Entangled Sensor Network. *arXiv preprint arXiv:1901.09566*, 2019.
- [9] Tyson Jones and Simon C Benjamin. Quantum compilation and circuit optimisation via energy dissipation. *arXiv preprint arXiv:1811.03147*, 2018.

- [10] Kentaro Heya, Yasunari Suzuki, Yasunobu Nakamura, and Keisuke Fujii. Variational Quantum Gate Optimization. *arXiv preprint arXiv:1810.12745*, 2018.
- [11] Vittorio Giovannetti, Seth Lloyd, and Lorenzo Maccone. Quantum-enhanced measurements: beating the standard quantum limit. *Science*, 306(5700):1330–1336, 2004.
- [12] Luca Pezzè, Augusto Smerzi, Markus K. Oberthaler, Roman Schmied, and Philipp Treutlein. Quantum metrology with nonclassical states of atomic ensembles. *Rev. Mod. Phys.*, 90:035005, Sep 2018.
- [13] Vittorio Giovannetti, Seth Lloyd, and Lorenzo Maccone. Advances in quantum metrology. *Nat. Phot.*, 5(4):222, 2011.
- [14] Géza Tóth and Iagoba Apellaniz. Quantum metrology from a quantum information science perspective. *J. Phys. A: Math. Theor.*, 47(42):424006, oct 2014.
- [15] Malcolm H Levitt. *Spin dynamics: basics of nuclear magnetic resonance*. John Wiley & Sons, Chichester, 2001.
- [16] David Le Sage, Koji Arai, David R Glenn, Stephen J DeVience, Linh M Pham, Lilah Rahn-Lee, Mikhail D Lukin, Amir Yacoby, Arash Komeili, and Ronald L Walsworth. Optical magnetic imaging of living cells. *Nature*, 496(7446):486, 2013.
- [17] Edward Ramsden. *Hall-effect sensors: theory and application*. Elsevier, 2011.
- [18] Martin E Huber, Nicholas C Koshnick, Hendrik Bluhm, Leonard J Archuleta, Tommy Azua, Per G Björnsson, Brian W Gardner, Sean T Halloran, Erik A Lucero, and Kathryn A Moler. Gradiometric micro-SQUID susceptometer for scanning measurements of mesoscopic samples. *Rev. Sci. Instr.*, 79(5):053704, 2008.
- [19] Martino Poggio and Christian L Degen. Force-detected nuclear magnetic resonance: recent advances and future challenges. *Nanotech.*, 21(34):342001, 2010.
- [20] Mustafa Bal, Chunqing Deng, Jean-Luc Orgiazzi, FR Ong, and Adrian Lupascu. Ultrasensitive magnetic field detection using a single artificial atom. *Nat. Comm.*, 3:1324, 2012.
- [21] Thomas Wolf, Philipp Neumann, Kazuo Nakamura, Hitoshi Sumiya, Takeshi Ohshima, Junichi Isoya, and Jörg Wrachtrup. Subpicotesla diamond magnetometry. *Phys. Rev. X*, 5(4):041001, 2015.
- [22] Toyofumi Ishikawa, Kai-Mei C Fu, Charles Santori, Victor M Acosta, Raymond G Beausoleil, Hideyuki Watanabe, Shinichi Shikata, and Kohei M Itoh. Optical and spin coherence properties of nitrogen-vacancy centers placed in a 100 nm thick isotopically purified diamond layer. *Nano Lett.*, 12(4):2083–2087, 2012.
- [23] S. F. Huelga, C. Macchiavello, T. Pellizzari, A. K. Ekert, M. B. Plenio, and J. I. Cirac. Improvement of Frequency Standards with Quantum Entanglement. *Phys. Rev. Lett.*, 79:3865–3868, Nov 1997.
- [24] Jan Kołodyński and Rafał Demkowicz-Dobrzański. Efficient tools for quantum metrology with uncorrelated noise. *New J. Phys.*, 15(7):073043, jul 2013.
- [25] Rafał Demkowicz-Dobrzański, Jan Kołodyński, and Mădălin Guță. The elusive Heisenberg limit in quantum-enhanced metrology. *Nat. Comm.*, 3:1063, 2012.
- [26] Yuichiro Matsuzaki, Simon C. Benjamin, and Joseph Fitzsimons. Magnetic field sensing beyond the standard quantum limit under the effect of decoherence. *Phys. Rev. A*, 84:012103, Jul 2011.
- [27] Alex W. Chin, Susana F. Huelga, and Martin B. Plenio. Quantum Metrology in Non-Markovian Environments. *Phys. Rev. Lett.*, 109:233601, Dec 2012.
- [28] Roei Ozeri. Heisenberg limited metrology using quantum error-correction codes. *arXiv preprint arXiv:1310.3432*, 2013.
- [29] G. Arrad, Y. Vinkler, D. Aharonov, and A. Retzker. Increasing Sensing Resolution with Error Correction. *Phys. Rev. Lett.*, 112:150801, Apr 2014.
- [30] W. Dür, M. Skotiniotis, F. Fröwis, and B. Kraus. Improved Quantum Metrology Using Quantum Error Correction. *Phys. Rev. Lett.*, 112:080801, Feb 2014.
- [31] E. M. Kessler, I. Lovchinsky, A. O. Sushkov, and M. D. Lukin. Quantum Error Correction for Metrology. *Phys. Rev. Lett.*, 112:150802, Apr 2014.

- [32] David A. Herrera-Martí, Tuvia Gefen, Dorit Aharonov, Nadav Katz, and Alex Retzker. Quantum Error-Correction-Enhanced Magnetometer Overcoming the Limit Imposed by Relaxation. *Phys. Rev. Lett.*, 115:200501, Nov 2015.
- [33] Martin B. Plenio and Susana F. Huelga. Sensing in the presence of an observed environment. *Phys. Rev. A*, 93:032123, Mar 2016.
- [34] Debbie W. Leung, M. A. Nielsen, Isaac L. Chuang, and Yoshihisa Yamamoto. Approximate quantum error correction can lead to better codes. *Phys. Rev. A*, 56:2567–2573, Oct 1997.
- [35] S. Taghavi, R. L. Kosut, and D. A. Lidar. Channel-Optimized Quantum Error Correction. *IEEE Transactions on Information Theory*, 56(3):1461–1473, March 2010.
- [36] Peter D Johnson, Jonathan Romero, Jonathan Olson, Yudong Cao, and Alán Aspuru-Guzik. QVECTOR: an algorithm for device-tailored quantum error correction. *arXiv preprint arXiv:1711.02249*, 2017.
- [37] Anil Shaji and Carlton M. Caves. Qubit metrology and decoherence. *Phys. Rev. A*, 76:032111, Sep 2007.
- [38] Duger Ulam-Orgikh and Masahiro Kitagawa. Spin squeezing and decoherence limit in Ramsey spectroscopy. *Phys. Rev. A*, 64:052106, Oct 2001.
- [39] BM Escher, RL de Matos Filho, and L Davidovich. General framework for estimating the ultimate precision limit in noisy quantum-enhanced metrology. *Nat. Phys.*, 7(5):406, 2011.
- [40] F Frwis and M Skotiniotis and B Kraus and W Dr. Optimal quantum states for frequency estimation. *New J. Phys.*, 16(8):083010, aug 2014.
- [41] Marcin Jarzyna and Rafał Demkowicz-Dobrzański. Matrix Product States for Quantum Metrology. *Phys. Rev. Lett.*, 110:240405, Jun 2013.
- [42] M. Oszmaniec, R. Augusiak, C. Gogolin, J. Kołodyński, A. Acín, and M. Lewenstein. Random Bosonic States for Robust Quantum Metrology. *Phys. Rev. X*, 6:041044, Dec 2016.
- [43] Yingkai Ouyang, Nathan Shettell, and Damian Markham. Robust quantum metrology with explicit symmetric states. *arXiv preprint arXiv:1908.02378*, 2019.
- [44] Michael A. Nielsen and Isaac L. Chuang. *Quantum Computation and Quantum Information: 10th Anniversary Edition*. Cambridge University Press, New York, NY, USA, 10th edition, 2011.
- [45] Samuel L. Braunstein and Carlton M. Caves. Statistical distance and the geometry of quantum states. *Phys. Rev. Lett.*, 72:3439–3443, May 1994.
- [46] C.W. Helstrom. Minimum mean-squared error of estimates in quantum statistics. *Phys. Lett. A*, 25(2):101 – 102, 1967.
- [47] Jing Liu, Haidong Yuan, Xiao-Ming Lu, and Xiaoguang Wang. Quantum Fisher information matrix and multiparameter estimation. *J. Phys. A: Math. Theo.*, 2019.
- [48] Jing Liu, Xiao-Xing Jing, Wei Zhong, and Xiao-Guang Wang. Quantum Fisher Information for Density Matrices with Arbitrary Ranks. *Comm. Theor. Phys.*, 61(1):45–50, jan 2014.
- [49] Michael M. Wolf and J. Ignacio Cirac. Dividing Quantum Channels. *Comm. Math. Phys.*, 279(1):147–168, Apr 2008.
- [50] LV Denisov. Infinitely divisible markov mappings in quantum probability theory. *Theory of Probability & Its Applications*, 33(2):392–395, 1989.
- [51] Tyson Jones, Anna Brown, Ian Bush, and Simon C Benjamin. QuEST and high performance simulation of quantum computers. *Sci. Rep.*, 9(1):10736, 2019.
- [52] Jian Ma, Xiaoguang Wang, C.P. Sun, and Franco Nori. Quantum spin squeezing. *Phys. Rep.*, 509(2):89 – 165, 2011.
- [53] Yingkai Ouyang, Nathan Shettell, and Damian Markham. Robust quantum metrology with explicit symmetric states. *arXiv preprint arXiv:1908.02378*, 2019.
- [54] John K Stockton, J. M. Geremia, Andrew C Doherty, and Hideo Mabuchi. Characterizing the entanglement of symmetric many-particle spin-1/2 systems. *Phys. Rev. A*, 67(2):022112, 2003.
- [55] Jun J. Sakurai. *Modern Quantum Mechanics*. Addison-Wesley, Reading, rev. edition, 1994.
- [56] Julian Schwinger. On Angular Momentum,. In L. C. Biedenharn and H. Van Dam, editors, *Quantum Theory of Angular Momentum*, pages 229–279. Academic Press, New York, 1965.

- [57] P. J. J. O'Malley, R. Babbush, I. D. Kivlichan, J. Romero, J. R. McClean, R. Barends, J. Kelly, P. Roushan, A. Tranter, N. Ding, B. Campbell, Y. Chen, Z. Chen, B. Chiaro, A. Dunsworth, A. G. Fowler, E. Jeffrey, E. Lucero, A. Megrant, J. Y. Mutus, M. Neeley, C. Neill, C. Quintana, D. Sank, A. Vainsencher, J. Wenner, T. C. White, P. V. Coveney, P. J. Love, H. Neven, A. Aspuru-Guzik, and J. M. Martinis. Scalable Quantum Simulation of Molecular Energies. *Phys. Rev. X*, 6:031007, Jul 2016.
- [58] Patrick Rebentrost, Maria Schuld, Leonard Wossnig, Francesco Petruccione, and Seth Lloyd. Quantum gradient descent and Newton's method for constrained polynomial optimization. *New J. Phys.*, 21(7):073023, jul 2019.
- [59] Ryan Sweke, Frederik Wilde, Johannes Meyer, Maria Schuld, Paul K Fährmann, Barthélémy Meynard-Piganeau, and Jens Eisert. Stochastic gradient descent for hybrid quantum-classical optimization. *arXiv preprint arXiv:1910.01155*, 2019.
- [60] Jonas M Kübler, Andrew Arrasmith, Lukasz Cincio, and Patrick J Coles. An adaptive optimizer for measurement-frugal variational algorithms. *arXiv preprint arXiv:1909.09083*, 2019.
- [61] Bálint Koczor and Simon C Benjamin. Quantum natural gradient generalised to non-unitary circuits. *arXiv preprint arXiv:1912.08660*, 2019.
- [62] Ilya Loshchilov, Marc Schoenauer, and Michèle Sebag. Adaptive coordinate descent. In *Proceedings of the 13th annual conference on Genetic and evolutionary computation*, pages 885–892, 2011.
- [63] GitHub repository. *Variational-State-Quantum-Metrology*, 2019. <https://github.com/QTechTheory/Variational-State-Quantum-Metrology>.
- [64] Akio Fujiwara and Hiroshi Imai. A fibre bundle over manifolds of quantum channels and its application to quantum statistics. *J. Phys. A: Math. Theor.*, 41(25):255304, may 2008.
- [65] Timothy F. Havel. Robust procedures for converting among Lindblad, Kraus and matrix representations of quantum dynamical semigroups. *J. Math. Phys.*, 44(2):534–557, 2003.
- [66] G. E. Uhlenbeck and L. S. Ornstein. On the Theory of the Brownian Motion. *Phys. Rev.*, 36:823–841, Sep 1930.
- [67] Ting Yu and J.H. Eberly. Entanglement evolution in a non-Markovian environment. *Optics Comm.*, 283(5):676 – 680, 2010.
- [68] David A. Meyer and Nolan R. Wallach. Global entanglement in multiparticle systems. *J. Math. Phys.*, 43(9):4273–4278, 2002.
- [69] Gavin K Brennen. An observable measure of entanglement for pure states of multi-qubit systems. *arXiv preprint quant-ph/0305094*, 2003.
- [70] M Enríquez, I Wintrowicz, and Karol Życzkowski. Maximally entangled multipartite states: a brief survey. In *J. Phys.: Conf. Ser.*, volume 698, page 012003. IOP Publishing, 2016.
- [71] G. S. Agarwal. Relation between atomic coherent-state representation, state multipoles, and generalized phase-space distributions. *Phys. Rev. A*, 24:2889–2896, 1981.
- [72] C. Brif and A. Mann. Phase-space formulation of quantum mechanics and quantum-state reconstruction for physical systems with Lie-group symmetries. *Phys. Rev. A*, 59(2):971–987, 1999.
- [73] Bálint Koczor, Robert Zeier, and Steffen J. Glaser. Continuous phase-space representations for finite-dimensional quantum states and their tomography. *Phys. Rev. A*, 101:022318, Feb 2020.
- [74] Bálint Koczor, Robert Zeier, and Steffen J. Glaser. Continuous phase spaces and the time evolution of spins: star products and spin-weighted spherical harmonics. *J. Phys. A.*, 52(5):055302, 2019. (*Preprint arXiv:1808.02697*).
- [75] Bálint Koczor, Robert Zeier, and Steffen J. Glaser. Time evolution of coupled spin systems in a generalized Wigner representation. *Ann. Phys.*, 408(September):1–50, 2019.
- [76] Bálint Koczor. *On phase-space representations of spin systems and their relations to infinite-dimensional quantum states*. Dissertation, Technische Universität München, Munich, 2019.
- [77] A. Grossmann. Parity operator and quantization of  $\delta$ -functions. *Comm. Math. Phys.*, 48(3):191–194, 1976.

- [78] Bálint Koczor, Frederik vom Ende, Maurice A. de Gosson, Steffen J Glaser, and Robert Zeier. Phase Spaces, Parity Operators, and the Born-Jordan Distribution, 2018. (*Preprint arXiv:1811.05872*).
- [79] Todd Tilma, Mark J Everitt, John H Samson, William J Munro, and Kae Nemoto. Wigner Functions for Arbitrary Quantum Systems. *Phys. Rev. Lett.*, 117(18):180401, 2016.
- [80] Rami Barends, Julian Kelly, Anthony Megrant, Andrzej Veitia, Daniel Sank, Evan Jeffrey, Ted C White, Josh Mutus, Austin G Fowler, Brooks Campbell, et al. Superconducting quantum circuits at the surface code threshold for fault tolerance. *Nature*, 508(7497):500, 2014.
- [81] Matthew D Reed, Leonardo DiCarlo, Simon E Nigg, Luyan Sun, Luigi Frunzio, Steven M Girvin, and Robert J Schoelkopf. Realization of three-qubit quantum error correction with superconducting circuits. *Nature*, 482(7385):382, 2012.
- [82] Julian Kelly, Rami Barends, Austin G Fowler, Anthony Megrant, Evan Jeffrey, Theodore C White, Daniel Sank, Josh Y Mutus, Brooks Campbell, Yu Chen, et al. State preservation by repetitive error detection in a superconducting quantum circuit. *Nature*, 519(7541):66, 2015.
- [83] John Clarke and Frank K Wilhelm. Superconducting quantum bits. *Nature*, 453(7198):1031, 2008.
- [84] Hiraku Toida, Yuichiro Matsuzaki, Kosuke Kakuyanagi, Xiaobo Zhu, William J Munro, Hiroshi Yamaguchi, and Shiro Saito. Electron paramagnetic resonance spectroscopy using a single artificial atom. *Comm. Phys.*, 2(1):33, 2019.
- [85] PA Knott. A search algorithm for quantum state engineering and metrology. *New J. Phys.*, 18(7):073033, 2016.
- [86] C. J. Ballance, T. P. Harty, N. M. Linke, M. A. Sepiol, and D. M. Lucas. High-Fidelity Quantum Logic Gates Using Trapped-Ion Hyperfine Qubits. *Phys. Rev. Lett.*, 117:060504, Aug 2016.